Article:
Sreenivasan, H., Adesanya, E., Niu, H. et al. (2021) Evidence of formation of an amorphous magnesium silicate (AMS) phase during alkali activation of (Na-Mg) aluminosilicate glasses. Cement and Concrete Research, 145. 106464. ISSN: 0008-8846

https://doi.org/10.1016/j.cemconres.2021.106464

Cement and Concrete Research 145 (2021) 106464

Contents lists available at ScienceDirect

Cement and Concrete Research

journal homepage: www.elsevier.com/locate/cemconres

Evidence of formation of an amorphous magnesium silicate (AMS) phase during alkali activation of (Na-Mg) aluminosilicate glasses

Harisankar Sreenivasan [a], Elijah Adesanya [a], He Niu [a], Priyadharshini Perumal [a], Anu M. Kantola [c], Ville-Veikko Telkki [c], Marko Huttula [b], Wei Cao [b], John L. Provis [d], Mirja Illikainen [a], Paivo Kinnunen [a,*]

[a] Fibre and Particle Engineering Research Unit, P.O. Box 4300, FI-90014, University of Oulu, Finland
[b] Nano and Molecular Systems Research Unit, P.O. Box 3000, FI-90014, University of Oulu, Finland
[c] NMR Research Unit, Faculty of Science, P.O. Box 3000, FI-90014, University of Oulu, Finland
[d] Department of Materials Science and Engineering, The University of Sheffield, Sir Robert Hadfield Building, Sheffield S1 3JD, United Kingdom

ARTICLE INFO

Keywords:
Fate of magnesium
Amorphous magnesium silicate phase
Geopolymers
Alkali activated materials
Hydrotalcite

ABSTRACT

There is some ambiguity regarding the fate of Mg during the alkali activation of Mg-rich precursors within the broader field of alkali activated materials (AAMs). The present work addresses this issue by studying the reaction products in AAMs synthesized from (Na-Mg) aluminosilicate glasses. Here, instead of magnesium silicate hydrate (M-S-H) phase, Mg exclusively forms an amorphous magnesium silicate (AMS) phase. Compared to M-S-H, AMS is a more depolymerized phase, which has not previously been well documented. The formation of AMS seems to be driven by the high charge density of the Mg cation which effectively stabilizes the depolymerized silicate species. We also show that the lack of hydrotalcite-group phases is due to aluminum depletion by zeolite formation. This work highlights the need to consider the existence of the AMS phase in Mg-containing AAMs, especially in complex systems, where its identification may be difficult.

1. Introduction

The synthesis of alkali-activated materials (AAMs) as cementitious binders involves alkaline activation of precursors such as blast furnace slag (BFS), coal fly ash, metakaolin, and others [1,2]. The main binder phase in the AAMs depends on the calcium content of the precursors: high-calcium precursors produces calcium aluminosilicate hydrate gel (C-A-S-H) as the main binder phase; low-calcium precursors yield an alkali aluminosilicate phase (N-A-S-H if sodium is the main alkali metal present), while intermediate-calcium and blended AAM systems result in a mixture of C-A-S-H and N-A-S-H phases [1]. Apart from silicon, aluminum and calcium, the precursors used for AAM synthesis sometimes contain a significant proportion of magnesium. In these cases, magnesium can considerably affect the phase assemblage formed during the alkali activation process, and hence can influence the final properties and applications of AAMs.

During the alkali activation, magnesium can possibly form the following phases: hydrotalcite-group minerals ($[Mg_{1-x}Al_xOH][OH, ½CO_3]\cdot mH_2O$), brucite ($Mg(OH)_2$), magnesium silicate hydrate (M-S-H), or magnesium (hydroxy-)carbonates. Each of these phases has its own implications for the structure, properties and applications of the AAMs. Increased hydrotalcite formation is known to reduce aluminum incorporation into the C-A-S-H phase, and appears to improve the mechanical strength of the AAMs [3]. AAMs with high contents of hydrotalcite have been observed to exhibit improved resistance to degradation associated with carbonation [4] and chloride attack [5]. Formation of brucite can lead to volumetric expansion of cementitious materials [6,7]. The M-S-H phase is known to have cementitious character and high mechanical strength [8], and it can be beneficial in applications of cementitious materials for immobilization and disposal of nuclear wastes [7,9,10]. If magnesium (hydroxy-)carbonates such as magnesite ($MgCO_3$), nesquehonite ($MgCO_3\cdot 3H_2O$), hydromagnesite ($Mg_5(CO_3)_4(OH)_2\cdot 4H_2O$), or dypingite ($Mg_5(CO_3)_4(OH)_2\cdot 5H_2O$) are formed in cementitious materials by uptake of atmospheric CO_2, it may further lower the carbon footprint, and the design of materials which act by this mechanism has been claimed as a route to make the cementitious materials sector more ecofriendly [7]. Considering the various ways in which magnesium-containing phases can influence the structure, properties and

* Corresponding author.
E-mail address: paivo.kinnunen@oulu.fi (P. Kinnunen).

https://doi.org/10.1016/j.cemconres.2021.106464
Received 13 November 2020; Received in revised form 14 February 2021; Accepted 9 April 2021
Available online 23 April 2021

application of AAMs, it is important to gain better insights into the fate of magnesium during alkali activation process.

The main products formed and the fate of magnesium during alkali activation of magnesium-rich precursors reported in the literature is summarized in Table 1. Note that this table is not exhaustive, and it is included here to show the variety of magnesium-rich precursors used in the context of alkali activation and the fate of magnesium in each. Hydrotalcite-group minerals (with varying Mg/Al and OH/CO_3 ratios, but discussed here together as a single class) are the most widely reported magnesium-containing phase, and are formed when a wide variety of magnesium-containing precursors and activators are used for AAM synthesis [4,11–20]. Alkali activation of high-magnesium nickel slags has been reported to form other Mg-containing phases including brucite, M-S-H and sodium magnesium aluminosilicate hydrate (N-M-A-S-H) [19,21]. There are also some studies where no specifically magnesium-containing phases are detected, although the precursors used are rich in magnesium [20,22,23]. Walling et al. [20] activated a mixture of SiO_2 and $Mg(OH)_2$ with $NaAlO_2$ and found no newly-formed magnesium-containing phases when the Si:Al ratio was high, and found hydrotalcite when the Si:Al ratio was low. The equivalent MgO content of those systems varied from 27 to 34 wt%, and the authors reported that $Mg(OH)_2$ was exhibiting limited reactivity. However, it would be interesting to understand why $Mg(OH)_2$ reacts to form hydrotalcite at low Si:Al ratio, but not at high Si:Al ratio. Kinnunen et al. [22] activated a mix of stone wool and fly ash using a solution of NaOH & $NaAlO_2$ and observed no distinct magnesium-containing phases; the MgO content of their mixed precursors varied from 9.2 to 12.2 wt%. Zhang et al. [23] synthesized AAMs by sodium silicate activation of BFS and detected no distinct magnesium-containing phases in the final product, although the precursor contained 9.3 wt% of MgO. Considering the results of these studies, it is interesting to consider why no evident magnesium-containing phase is formed in certain systems with high magnesium content. And indeed, whether it is possible that a magnesium-containing phase was formed, but the phase in question was such that it could not be directly detected with the methods used in those studies. Answering these questions may be made possible through studies based on simple magnesium-containing precursors such as Na—Mg aluminosilicate glasses.

Table 1
Main products formed and the fate of Mg during alkali activation of Mg-rich precursors, according to selected studies.

Precursors	Mix design (mole ratio): Si:Al:Mg:Ca:Na	Activator	Fate of Mg	Main product	Ref.
BFS	1: (0.33–0.43): (0.21–0.26): (0.99–1.27): (0.18–0.22)	NS_x	HT	C-A-S-H	[4]
BFS	1: 0.40: 0.29: 1.00: 0.09	N$	HT	C-A-S-H	[11]
BFS + MK	1: 0.60: 0.23: 0.96: 0.17	NH	HT	C-A-S-H	[12]
BFS+ FA	1: 0.43: (0.23–0.61): 0.77: (0.16–0.34)	Nc	HT	C-A-S-H	[13]
BFS + Mg $(OH)_2$	1: 0.44: (0.34–4.07): 1.24: (0.36–0.82)	Nc	HT	C-A-S-H	[14]
BFS + MgO	1: 0.36: (0.45–0.54): 1.38: (0.15–0.24)	NH	HT	C-A-S-H	[15]
Stone wool	1: 0.45: 0.41: 0.41: 1.94	NH	HT	C-A-S-H	[16]
Synthetic precursor powders	1: (0.05–0.15): (0.05–0.29): (0.70–1.15): (0.03–0.08)	NS_x	HT	C-A-S-H	[17]
Synthetic slags	1: (0.44–0.53): (0.01–0.70): (1.02–1.61): 0.26	NH	HT	C-A-S-H	[18]
High Mg NS	1: (0.07–0.15): (0.73–1.08): (0.07–0.21): (0.47–0.51)	NH	M-S-H + HT + B	M-S-H	[19]
High Mg NS + FA	1: (0.33–0.62): (0.03–0.43): (0.08–0.13): (0.22–0.30)	NS_x	N-M-A-S	N-M-A-S	[21]
SiO_2 + Mg $(OH)_2$ + $NaAlO_2$	1: 1.50: 3.00: 0: 1.50	NA	HT	Zeolite	[20]
SiO_2 + Mg $(OH)_2$ + $NaAlO_2$	1: (0.60–1.00): (1.20–2.00): 0: (0.60–1.00)	NA	–	Zeolite	[20]
Stone wool wool + FA	1: (0.46–0.80): (0.18–0.43): (0.18–0.38): (0.39–1.81)	NH + NA	–	C-A-S-H	[22]
BFS	1: 0.48: 0.40: 1.21: 0.16	NS_x	–	C-A-S-H	[23]

Note: a) For column 1: BFS-blast furnace slag; MK-metakaolin; FA-fly ash; NS-nickel slag.
b) For column 3: NS_x-sodium silicate; NH-sodium hydroxide; NA-sodium aluminate; N$-sodium sulfate; Nc-sodium carbonate.
c) For column 4: HT-hydrotalcite-like phase; B-brucite; M-S-H - magnesium silicate hydrate; N-M-A-S – sodium magnesium aluminosilicate hydrate.
d) For column 5: C-A-S-H – calcium aluminosilicate hydrate; M-S-H - magnesium silicate hydrate; N-M-A-S – magnesium aluminosilicate hydrate.

This work focuses on understanding the fate of magnesium during the alkali activation of (Na—Mg) aluminosilicate glasses. Several glasses with compositions ($(Na_2O)_{0.8-x}(MgO)_x$ $(Al_2O_3)_{0.2}(SiO_2)$; $0.8 \geq x \geq 0$) were prepared and alkali activated (liquid to solid mass ratio, L/S, = 0.35) with NaOH to produce AAMs, which were cured for 1 year. Glass samples were also subjected to an alkaline dissolution experiment (L/S = 40) to understand the fate of magnesium in the precipitated phase. Sample characterization involved X-ray diffraction (XRD), ^{29}Si magic angle spinning nuclear magnetic resonance (MAS NMR) spectroscopy, ^{29}Al MAS NMR, scanning electron microscopy (SEM), and thermogravimetry-mass spectrometry (TG-MS) analysis.

2. Materials and methods

2.1. Materials

For the glass synthesis, the following precursors were used: SiO_2 (Alfa Aesar; purity 99.5%), Al_2O_3 (Sigma-Aldrich; purity 99.5%), Na_2CO_3 (Sigma-Aldrich; purity 99.0%), and MgO (Sigma-Aldrich: purity 99.0%). Activation solution (6 M NaOH) was prepared using NaOH (Merck-Germany; purity >99%). Deionized water was used wherever needed.

2.2. Methods

2.2.1. Preparation of glasses

A series of ten Na—Mg aluminosilicate glasses (compositions shown in Table 2) were prepared. The detailed procedure was described

Table 2
Composition of (Na—Mg) aluminosilicate glasses.

Sample code	Formula of glass	MgO (wt%)	Nominal NBO/Si
G1	$Na_{1.60}Al_{0.40}Si_{1.00}O_{3.40}$	0	1.25
G2	$Na_{1.42}Mg_{0.09}Al_{0.40}Si_{1.00}O_{3.40}$	2.8	
G3	$Na_{1.25}Mg_{0.18}Al_{0.40}Si_{1.00}O_{3.40}$	5.6	
G4	$Na_{1.07}Mg_{0.26}Al_{0.40}Si_{1.00}O_{3.40}$	8.6	
G5	$Na_{0.90}Mg_{0.35}Al_{0.40}Si_{1.00}O_{3.40}$	11.6	
G6	$Na_{0.72}Mg_{0.44}Al_{0.40}Si_{1.00}O_{3.40}$	14.7	
G7	$Na_{0.54}Mg_{0.53}Al_{0.40}Si_{1.00}O_{3.40}$	18.0	
G8	$Na_{0.37}Mg_{0.62}Al_{0.40}Si_{1.00}O_{3.40}$	21.3	
G9	$Na_{0.19}Mg_{0.70}Al_{0.40}Si_{1.00}O_{3.40}$	24.8	
G10	$Mg_{0.80}Al_{0.40}Si_{1.00}O_{3.40}$	28.3	

NBO = non-bridging oxygen.

previously [24].

2.2.2. Synthesis of AAMs from glasses (L/S = 0.35)

The glass precursor (100 g) was mixed with the activating solution (35 g of 6 M NaOH solution) in a high shear mixer (IKA EUROSTAR 20) at 3000 rpm for 30 min. The mixture was then introduced into cylindrical plastic molds (25 mm height and 25 mm diameter) and sealed in plastic bags for curing at 40 °C for 1 day. After 1 day, the sealed plastic bags were kept at room temperature for 1 year. The AAM obtained from glass Gz is denoted as Az_1Y.

2.2.3. Alkaline dissolution experiments (L/S = 40)

The detailed procedure followed is explained in [25]. Briefly, 0.5 g of sample was mixed with 20 g of 6 M NaOH solution in a polypropylene bottle. The bottle was subjected to a shaking motion (2.5 Hz) for 1 day at 23 ± 0.5 °C using a horizontal shaking table (IKA KS 260 orbital shaker). After 1 day, the solution was filtered with nylon filter paper (0.45 μm). The solid residue was washed with deionized water multiple times, and then dried in a desiccator at room temperature for 2 days. The residue remaining after the dissolution experiment of glass Gz is denoted as Rz_1D.

2.2.4. Characterization techniques

The compressive strength of the AAMs was determined using a Zwick 100 machine which employed a loading force ramp of 2.4 kN/s until failure. The milling of samples (1500 rpm for 3 min) was performed using a vibratory disc mill (Retsch RS 200) to obtain powdered samples for further characterization.

XRD pattern of powdered samples were recorded using a Rigaku SmartLab 9 kW XRD instrument. The process employed Co Kα radiation (Kα1 = 1.78892 Å; Kα2 = 1.79278 Å; Kα1/Kα2 = 0.5), a scan rate of 3°/min between 5° and 85° 2θ, and 0.02°/step. For the purpose of phase identification, X'pert HighScore Plus (PANalytical) software was used, with the Powder Diffraction File (PDF) database.

The solid-state MAS NMR spectra were measured using a Bruker Avance III 300 spectrometer. The samples were packed inside 7 mm zirconia rotors and the spinning frequency was 7 kHz. The frequency of the ^{29}Si measurements was 59.65 MHz, and 8192 scans were acquired with a repetition time of 3 s (pulse was 5.5 μs, 90° pulse). Tetramethylsilane was used as an external standard for referencing the chemical shifts at 0 ppm. The frequency of the ^{27}Al measurements was 78.24 MHz, and 2048 scans were acquired with a repetition time of 2 s (pulse was 1.0 μs, 30° pulse). Chemical shifts were referenced to $Al(NO_3)_3$ as an external standard at 0 ppm.

Thermal analysis of the samples was carried out using a Netzsch STA 449 F3 TGA-DTA/DSC analyzer (Selb, Germany) coupled to a mass spectrometer (MS). The sample (20 mg), placed in an alumina crucible, was heated up to 700 °C at a heating rate of 10 °C min^{-1} under a nitrogen environment (purge rate 200 mL/min).

A Zeiss Ultra Plus field emission scanning electron microscope (FESEM) was used for recording the scanning electron microscopic (SEM) images of the samples. The microscope was equipped with an Oxford energy-dispersive X-ray spectroscopy (EDS) detector, and Aztec software was used for elemental mapping. During the sample preparation, crushed AAMs (after the strength test) was impregnated in epoxy resin. After the hardening of the resin over 1 day, the sample was polished using a diamond (0.25 μm) paste to obtain a smooth surface. The sample surface was coated with carbon to produce a conducting layer.

3. Results and discussion

3.1. Compressive strength of the AAMs

The AAM sample A1_1Y, synthesized from the sodium end-member of the aluminosilicate glass series, showed a compressive strength of 13 MPa after 1 year of curing, Fig. 1. As the magnesium content of the glass precursor increased, the compressive strength increased initially and reached a maximum of 25 MPa in the case of A3_1Y, but then compressive strength decreased at higher Mg content, to a minimum value of around 3 MPa in the case of A10_1Y. This trend in compressive strength, as illustrated in Fig. 1, appears to follow the trend in alkaline reactivity of the aluminosilicate glasses as determined previously [25]. In that previous study, the authors observed that alkaline reactivity of glasses increased initially with a rise in magnesium content of the glasses, reached a maximum value for G3, then reactivity decreased and dipped to a minimum value in case of G10 (see Supplementary Information, Figure SF1).

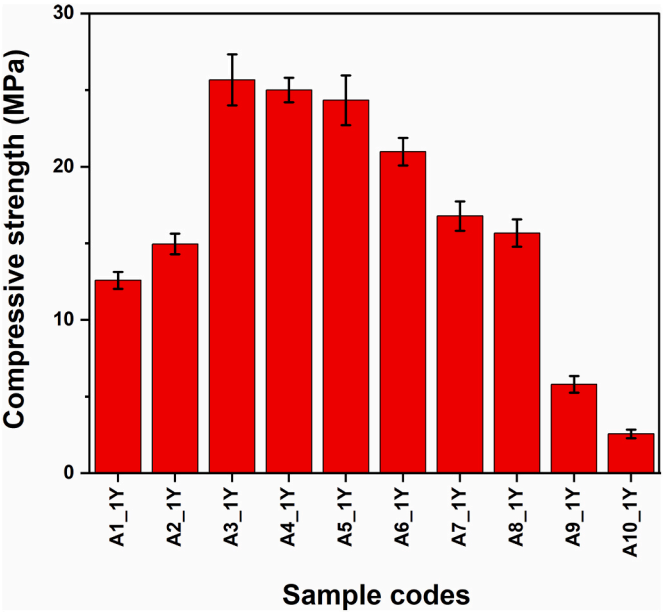

Fig. 1. Compressive strength of AAMs cured for 1 year.

The crushed samples (after compressive strength testing) were milled to obtain powders for further characterization. However, in case of samples A1_1Y, A2_1Y, and A3_1Y, the milling was not successful in producing powdered samples, since after grinding these samples transformed into sticky solid masses, rather than powders (Supplementary Information, Figure SF2). This may be due to the high sodium content of these AAMs. An additional cryogenic grinding step was attempted for these samples, but this also proved unsuccessful. As a result, powder characterization (XRD, NMR, SEM, TG-MS) could not be completed for these three samples.

3.2. XRD analysis

The XRD analysis of glass precursors (Fig. 2) revealed predominantly amorphous features along with minor crystalline contributions in certain samples. The sodium-rich glass sample, G4, showed presence of sodium carbonate (natrite, Na_2CO_3, PDF no: 04-011-4108). The formation of sodium carbonate is due to atmospheric carbonation of excess sodium present in the glass-forming melt. One of the glasses close to the magnesium endmember exhibited crystalline contributions originating from forsterite (Mg_2SiO_4, PDF no: 04-007-7321). Forsterite is known to show high resistance to vitrification processes [26]. Some glasses, especially those close to the magnesium endmember, also showed a peak at 52.3°, which can be attributed to iron (Fe, PDF no: 04-006-6419). The presence of iron in these samples is due to contamination during the grinding of samples in the vibratory disc mill, which employed a disc made of steel.

The XRD analysis of the AAMs produced from these glasses is shown in Fig. 3. The sample A4_1Y is dominated by LSX type zeolite (LSX_1, $Na_{96}Al_{96}Si_{96}O_{384}\cdot(H_2O)_{384.3}$, PDF no: 01-074-2534). The sample also

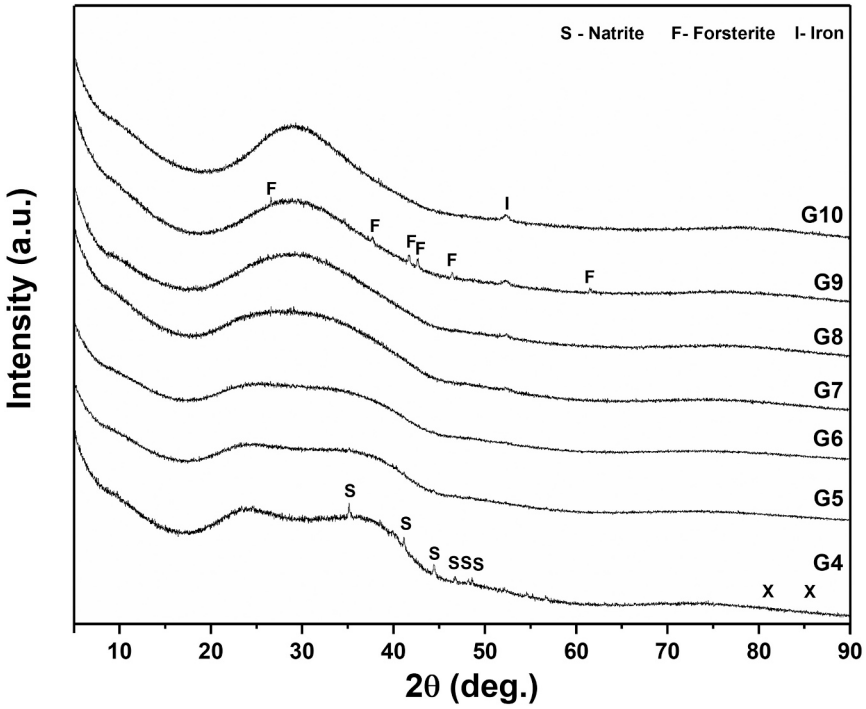

Fig. 2. XRD analysis of (Na—Mg) aluminosilicate glasses.
(Adapted from [24]).

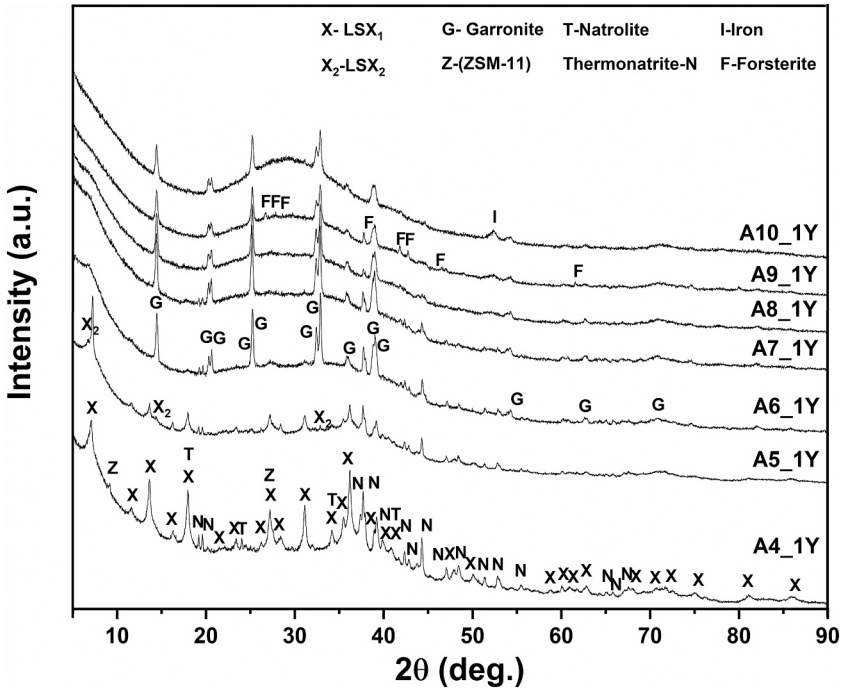

Fig. 3. XRD analysis of AAMs.

has minor contributions from zeolitic phases such as Natrolite ($Na_2Al_2Si_3O_{10}\cdot(H_2O)_2$, PDF No: 00-022-1224), and ZSM-11 ($Na_8Al_8Si_{40}O_{96}\cdot(H_2O)_8$, PDF no: 04-018-2360). A significant content of thermonatrite ($Na_2CO_3\cdot H_2O$, PDF no: 01-070-2148) is also present, due to atmospheric carbonation of excess sodium. The sample A5_1Y is also dominated by LSX type zeolite (LSX_1). It also contains thermonatrite and minor proportion of another LSX type zeolite (LSX_2, $Na_{23}Al_{23}Si_{25}O_{96}\cdot(H_2O)_x$, PDF No: 04-009-8639). The XRD pattern of the remaining AAMs (A6_1Y, A7_1Y, A8_1Y, A9_1Y, and A10_1Y) is dominated by the zeolitic phase garronite ($Na_4Al_4Si_4O_{16}\cdot(H_2O)_{7.6}$, PDF No: 04-011-7946). These samples also contain thermonatrite, the proportion of which decreases with reduction in sodium content of the AAMs, almost to zero in the case of A10_1Y. The sample A9_1Y shows the presence of forsterite which originates from the glass precursor G9 as mentioned above, which indicates that forsterite is inert towards alkali activation. The samples A8_1Y, A9_1Y, A10_1Y exhibit the presence of

iron; this originates from the iron contaminants in the respective glass precursors as well as potential contributions arising from grinding of AAMs in vibratory disc mill.

The XRD analysis of AAMs, as presented above, yielded no clue regarding the fate of magnesium during alkali activation. None of the samples showed any XRD reflections corresponding to any magnesium-bearing phases, such as hydrotalcite-group (Mg-layered double hydroxide, LDH) phases, which are the most widely reported form of magnesium in AAMs with considerable magnesium content. Another possibility is to consider the formation of M-S-H phases in these AAMs. XRD analysis of M-S-H phases produces broad features around 20°, 26° 36°, and 61° 2θ when employing Cu radiation [9,27]; as Co radiation was employed in this work, the M-S-H phase should thus produce broad features around 23°, 30°, 42°, and 71°, if it is formed in the AAMs. However, none of the AAMs showed any broad features around those regions in their XRD patterns. This means that no M-S-H phase is formed in these AAMs, or so little that is undetectable using XRD. This is in agreement with observations by Walling et al. [20], who also studied AAMs in the system Na_2O-MgO-Al_2O_3-SiO_2-H_2O under very highly alkaline conditions. Those authors concluded that there was no evidence of M-S-H phase formation when a mixture of SiO_2 and $Mg(OH)_2$ was activated with $NaAlO_2$, even though the AAMs were cured for up to 2 years.

Despite the apparent absence of magnesium-bearing crystalline phases in the alkali activated Mg-aluminosilicate glasses, such magnesium-bearing precipitates were visible in alkali dissolution residues of the same glasses at high L/S ratio. The XRD analysis of solid residues obtained during alkali dissolution of glasses are shown in Fig. 4. The data collected for all samples exhibit strong reflections belonging to a hydrotalcite-group phase (quintinite, $Mg_{0.67}Al_{0.33}(CO_3)_{0.17}(OH)_2(H_2O)_{0.5}$, PDF No: 04-015-4253). The intensities of the reflections of this phase grow as the magnesium content of the precursor glass increases. The diffractogram of sample R9_1D also contains reflections of forsterite, consistent with the statement above that forsterite is inert towards alkali activation. The reflections of iron (Fe, PDF no: 04-006-6419) are present in samples e.g. R8_1D, R9_1D and R10_1D.

During the alkali dissolution experiments, due to the high alkalinity of the solution as well the relatively high L/S (40), both silicon and aluminum readily dissolve in the solution. This can be clearly understood from the analysis of the solid residue (R1_1D) obtained from the dissolution of G1, the aluminosilicate glass with no magnesium content (refer Supplementary Information, S3 & S4). The XRD analysis of R1_1D did not show formation of any crystalline precipitate phase during alkali dissolution (refer Supplementary Information, Fig. SF3). The TEM analysis of R1_1D (refer Supplementary Information, Fig. SF4) showed corroded glass particles with no evidence of either crystalline or disordered precipitate phases around them. This means that during alkali dissolution of G1, the silicon and aluminum do not form any precipitate and hence, they preferably dissolve in the highly alkaline solution. Conversely, during the alkali dissolution of all glasses with magnesium (G2 to G10), magnesium is precipitated as hydrotalcite by also incorporating aluminum. Hydrotalcite is the only precipitating phase, and there is no contribution of silicon towards precipitate formation. This is supported by the XRD analysis (refer Supplementary Information, Fig. SF3) and TEM analysis (refer Supplementary Information, Fig. SF4) of the solid residues.

The following conclusions can be made from the XRD analysis of AAMs. During the synthesis of AAMs, the alkalinity (6 M NaOH) of the activation solution used is same as that used in the dissolution experiment. However, the L/S used in AAMs synthesis is 0.35, which is more than 100 times lower than the L/S used in the alkali dissolution experiment. Low L/S causes supersaturation of silicon, aluminum and magnesium with respect to both zeolite and hydrotalcite-group phases as the glasses dissolve. In this case, aluminum can be incorporated either into zeolite or hydrotalcite-group phases; in other words, both zeolite formation and hydrotalcite formation can compete for aluminum incorporation. It turns out that under these conditions, zeolite formation is kinetically favored, and aluminum preferentially incorporates along with silicon to form zeolites rather than incorporating along with magnesium to form hydrotalcite-group phases. Looking at the compositions of the glass precursors and the dominant zeolite phases in AAMs, the following information can be obtained. All the glass precursors used for the AAMs synthesis have a similar Si:Al ratio, 2.5. However, the dominant zeolite phases (LSX and garronite) formed in AAMs have an Si:

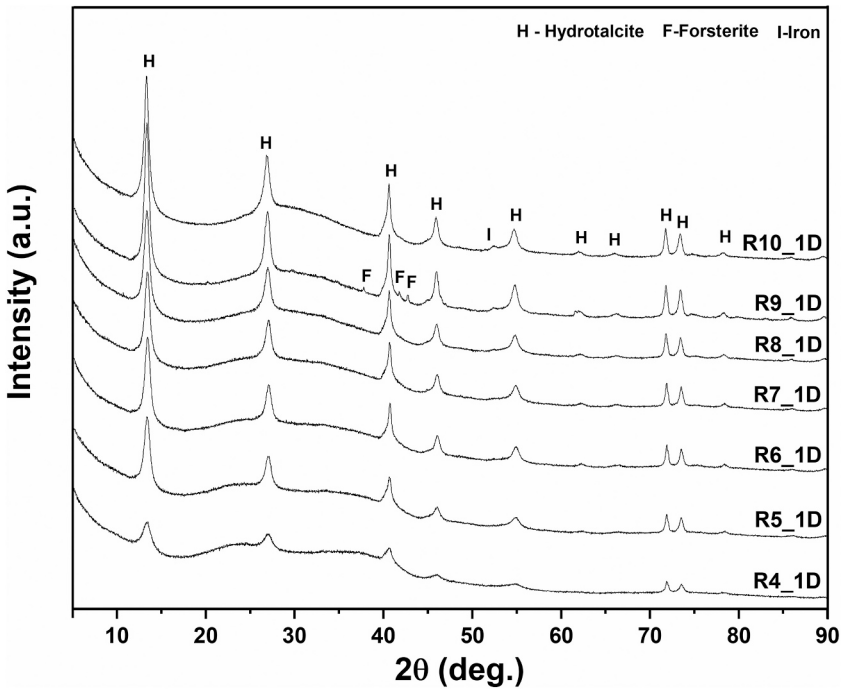

Fig. 4. XRD analysis of the solid residues obtained during alkaline dissolution experiments. (Adapted from [25]).

Al ratio of 1. This means that during the formation of these zeolites from glass precursors, aluminum is the limiting reactant. Hence, all the available aluminum is consumed in the formation of zeolites, thereby making no aluminum available for the hydrotalcite formation. In short, the absence of hydrotalcite phase in these particular AAMs is due to the fact that under the studied conditions, aluminum preferentially incorporates into zeolite phases rather than hydrotalcite-group phases.

The preferential incorporation of aluminum into zeolites, as concluded from this work, can possibly also explain the absence of hydrotalcite during alkali activation of some magnesium-rich precursors as reported in the literature (Table 1). Walling et al. [26] activated mixtures of SiO_2 and $Mg(OH)_2$ with $NaAlO_2$ and found that no hydrotalcite phase was formed when Si:Al is high, while hydrotalcite-group minerals did form when Si:Al was low. The dominant product in all the AAMs were zeolites, with Si:Al ratios from 1.00 to 1.67. The authors observed no hydrotalcite formation from precursor blends whose Si:Al ratio varied from 1.00 to 1.67, i.e., without a clear excess of aluminum (available after the formation of zeolite) to react with $Mg(OH)_2$ to form hydrotalcite. Hence, no hydrotalcite formed from those precursor compositions upon alkali activation. The only case in that study in which hydrotalcite-group minerals did form had a Si:Al ratio of 0.67. This system evidently possessed a significant excess of aluminum available after the formation of zeolites, which reacted with $Mg(OH)_2$ to form hydrotalcite-group phases.

Additionally, Kinnunen et al. [22] activated blends of silicate AAM precursors (stone wool + fly ash; 9.2 to 12.2 wt% MgO) using (NaOH + $NaAlO_2$) solution, and observed that no hydrotalcite phase was formed in the AAMs. Those authors found that along with a C-A-S-H phase, a significant proportion of zeolite ($Na_8(AlSiO_4)_6(OH)_2{\cdot}H_2O$) was formed during alkali activation. According to the logic presented above, this could be the reason for absence of the hydrotalcite phase in the AAMs. Correspondingly, Zhang et al. [23] synthesized AAMs by sodium silicate activation of BFS and detected no hydrotalcite phases in the final product (the MgO content of precursr is 9.3 wt%). Those authors observed that the AAMs consisted of C-A-S-H phases along with several crystalline aluminosilicate phases including natrolite, wairakaite, zoisite. The formation of multiple aluminosilicate phases in these AAMs could be the reason for absence of hydrotalcite phase.

3.3. ^{27}Al MAS NMR analysis of samples

The results of the ^{27}Al MAS NMR analysis of the glasses are shown in Fig. 5(a). The spectrum of the sample G4 has a broad resonance which spans from 0 ppm to 70 ppm with the maximum roughly at 55 pm. This represents predominantly tetrahedral aluminum (Al^{IV}) present in the aluminosilicate glasses [28]. As the magnesium content of the glasses increases, this signal gets broader. This broadening is due to the fact that the magnesium cation has relatively high charge density compared to sodium, and therefore can cause distortion of the aluminum environment [29]. The signal of the magnesium end member (G10) is much broader and has an irregular shape, indicating the highest distortion of aluminum environments and potential existence of considerable aluminum in pentahedral (Al^{V}) and octahedral (Al^{VI}) coordination environments.

The results of the ^{27}Al MAS NMR analysis of AAMs are shown in Fig. 5(b). The signal of A4_1Y is sharper (when compared to its precursor G4) and has its maximum around 58 ppm (while G4 had a maximum at 55 ppm). This represents the Al^{IV} aluminum environment of zeolitic species [30], as observed in the XRD analysis (Fig. 3). The spectrum of A4_1Y does not show any visible band in the octahedral region, and this indicates the absence of hydrotalcite-group phases. This agrees with the XRD analysis which also could not detect any hydrotalcite in A4_1Y. On moving from A4_1Y to A10_1Y, the signal becomes broader, which represent the decrease in reactivity of precursors on moving from G4 to G10. This follows the trend in compressive strength (Fig. 1), as well as the trend in the estimated reactivity of glasses (Refer supplementary information, Fig SF1). A small broad Al^{VI} band, roughly centered around 7 ppm, emerges gradually on moving from A4_1Y to A10_1Y. This band is attributed to the unreacted glass present in the AAMs. Note that none of the spectra indicated any possible presence of hydrotalcite-group

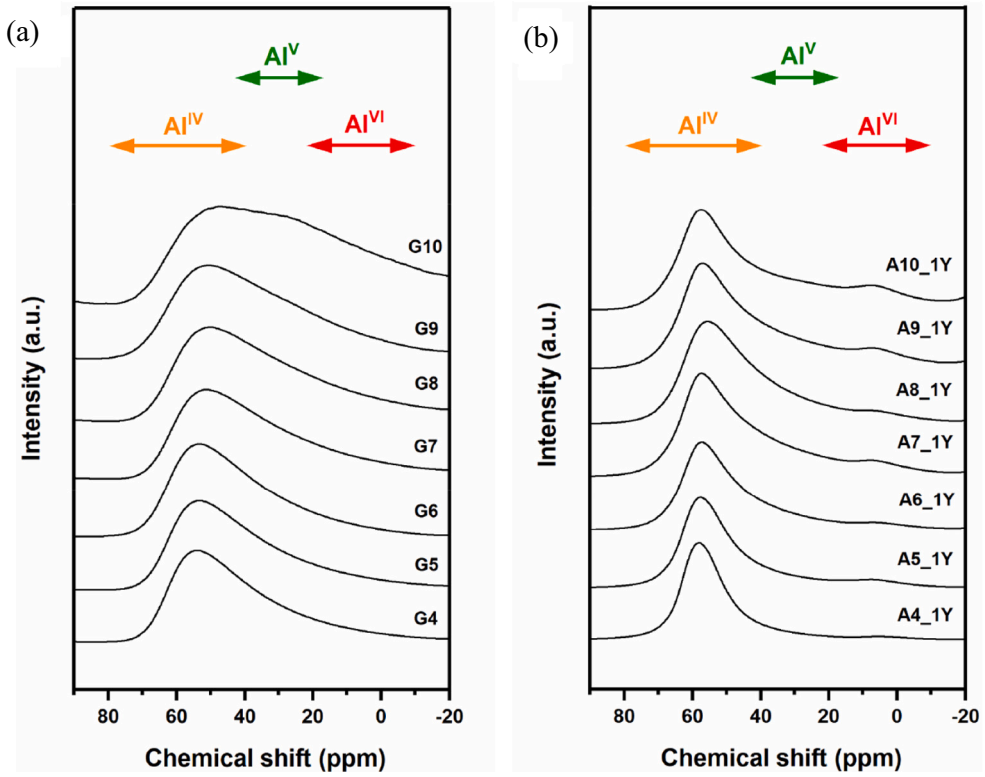

Fig. 5. ^{27}Al MAS NMR analysis of (a) glasses and (b) AAMs.

phases; if hydrotalcite was formed, it would have produced a sharper band in the octahedral region [31].

The results of the ^{27}Al MAS NMR analysis of solid residues after dissolution testing are shown in Fig. 6. The spectrum of R4_1D shows a broad band extending from 20 ppm to 70 ppm, with the maximum roughly at 55 ppm. This corresponds to the unreacted glass component. The spectrum has an Al^{VI} band at 8.2 ppm attributed to the hydrotalcite-group phase [32], which was also detected in the XRD analysis of this sample (Fig. 4). This Al^{VI} band grows in intensity on moving from R4_1D to R10_1D, indicating increased hydrotalcite formation, which agrees with the XRD analysis. Note that none of the spectra indicated the presence of any aluminosilicate phase in the residue; if an aluminosilicate phase was formed, it would have produced a sharper band in the tetrahedral region. This is also consistent with the XRD analysis (Fig. 4) and TEM analysis (refer Supplementary Information, S4) of the residues.

3.4. ^{29}Si MAS NMR analysis of samples

The ^{29}Si MAS NMR spectra of the AAMs were decomposed into Gaussian components representing various $Q^n(m\text{Al})$ silicate species. The decompositions were performed using Microsoft Excel in a manner similar to the previously reported studies [4,33]. During the decomposition, the minimum possible number of Gaussian components that can describe the overall spectrum in a satisfactorily manner were considered, and the full width at half maximum (FWHM) has been kept under 10 ppm. The chemical shifts were selected on the basis of information available in the literature [17,30,31,34]. The decomposition involved the following: (1) rescaling of unreacted glasses in a manner similar to previously reported study [33]; (2) formulation of six Gaussian components representing various $Q^n(m\text{Al})$ species of the product phase: Q^0 at −70.5 ppm, Q^1(0Al) at −77.0 ppm, Q^2(1Al) at −80.0 ppm, Q^2(0Al) at −83.0 ppm, Q^4(4Al) or Q^3(1Al) at −85.0 ppm, and Q^4(3Al) or Q^3(0Al) at −90.0 ppm. Q^0 at −70.5 ppm was chosen as there was appearance of a shoulder around −70.5 ppm in the ^{29}Si MAS NMR spectrum of A4_1Y, and a chemical shift around −70.5 ppm corresponds to Q^0 species according to the literature [31]. Q^1(0Al) at −77.0 ppm, Q^2(1Al) at −80.0 ppm, and Q^2(0Al) at −83.0 ppm were chosen based on the chemical shift assignments of Walkley et al. [17], who studied AAMs within the CaO-MgO-Na_2O-Al_2O_3-SiO_2 regime. Q^4(4Al) at −85.0 ppm and Q^4(3Al) at −90.0 ppm were chosen based on the chemical shifts pertaining to zeolitic phases [30]. Additionally, resonances at −85.0 ppm and −90.0 ppm may also be due to Q^3(1Al) and Q^3(0Al) species respectively [31]. The maximum variation allowed in chemical shift and FWHM values are ±0.5 ppm and ±0.7 ppm respectively (for individual values, refer Supplementary Information, S5). The decompositions of the spectra of A4_1Y and A10_1Y are shown in Fig. 7 as examples of the results obtained. The unreacted glass component is lower in A4_1Y than A10_Y, which agrees with the decrease in reactivity of glasses on moving from G4 to G10.

The product phase $Q^n(m\text{Al})$ distribution obtained through spectral decomposition is shown in Fig. 8. A4_1Y has the largest proportion of highly depolymerized silicate species (proportion of $Q^{0-2}(m\text{Al}) = 63\%$). On moving from A4_1Y to A10_1Y, the proportion of these species decreases and reaches a minimum in A10_1Y (proportion of $Q^{0-2}(m\text{Al}) = 13\%$). The proportion of highly polymerized silicate species, Q^{3-4}(mAl), is lowest in the case of A4_1Y (40%). The quantity of these species increases on moving from A4_1Y to A10_1Y and reaches a maximum in case of A10_1Y (87%). The Q^4(4Al) and Q^4(3Al) species present in the system can be attributed to the zeolite phases detected during the XRD analysis of AAMs (Fig. 3).

The ^{29}Si NMR spectral analysis can be used to rule out the existence of one of the possible fates of magnesium in AAMs: the M-S-H phase. The Q^3 species in M-S-H phase is known to produce distinct resonances between −92.4 and −96.7 ppm, which accounts for 40–70% of the total relative peak intensities of all the Q^n species belonging to the M-S-H phase, depending on the Mg/Si ratio [35]. However, during the ^{29}Si

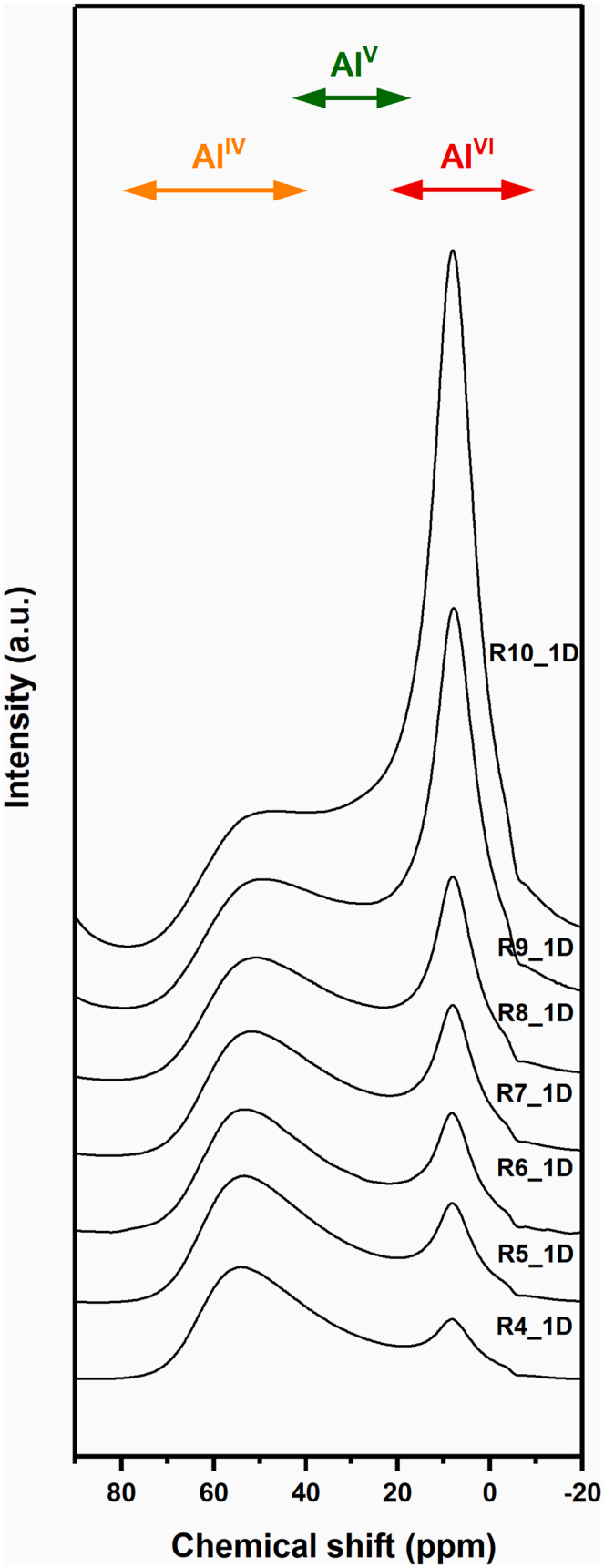

Fig. 6. ^{27}Al NMR analysis of solid residues from alkaline dissolution of glasses.

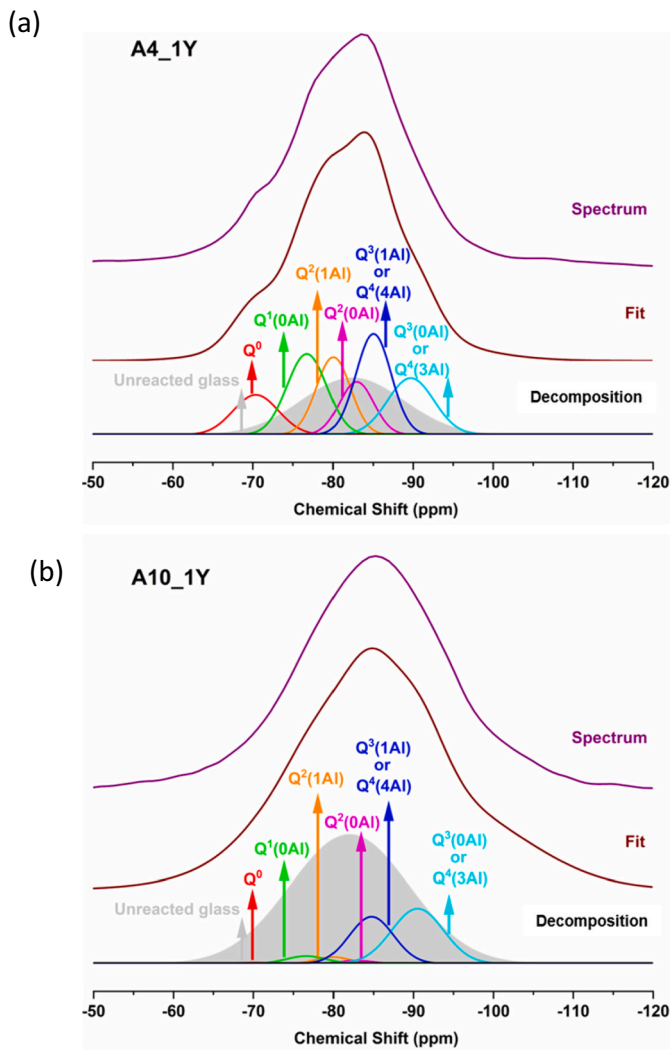

Fig. 7. ^{29}Si MAS NMR analysis of AAMs: Decomposition of spectrum of (a) A4_1Y and (b) A10_1Y.

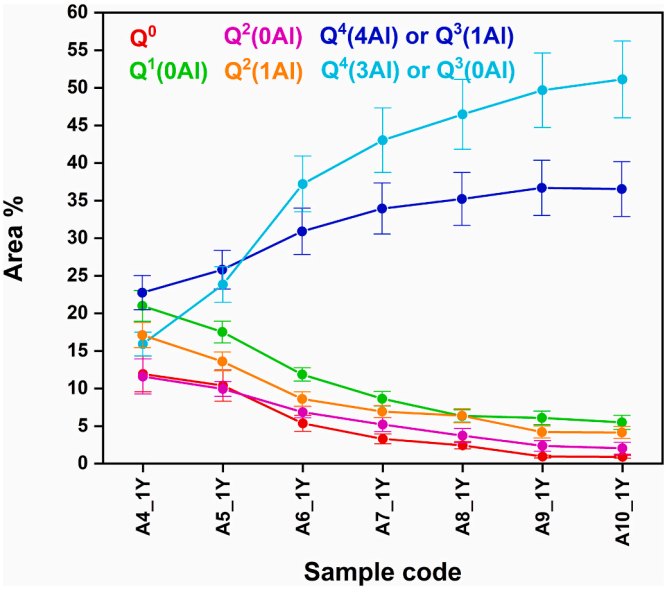

Fig. 8. Q^n distribution in product phase of AAMs.

NMR spectral analysis of AAMs in this work, the most negative chemical shift that could be reasonably assigned is −90.0 ppm. Hence, it can be concluded that a conventional M-S-H phase is not formed in AAMs. This agrees with XRD analysis which could not find any reflections pertaining to M-S-H phases in any of the AAMs (Fig. 3).

In order to further explore the potential presence of a conventional M-S-H phase in the AAMs, selected AAM samples have been subjected to ^{29}Si{^{1}H} CP/MAS NMR spectroscopic analysis (refer Supplementary Information, S6). In a conventional M-S-H phase, silicon occurs in proximity to hydrogen (which exists in the form of water). Hence, ^{29}Si{^{1}H} CP/MAS NMR spectroscopy, which involves transfer of polarization from hydrogen nuclei to silicon nuclei, will have higher sensitivity towards silicon species of a conventional M-S-H phase, when compared to ^{29}Si MAS NMR spectroscopy. The ^{29}Si{^{1}H} CP/MAS NMR spectral analysis of AAMs (refer Supplementary Information, S6.3.1) could not identify any distinct resonances in the region between −92.4 and −96.7 ppm, where the Q^3 species in conventional M-S-H would produce resonances. Additionally, a conventional M-S-H phase has been synthesized (from SiO_2 and MgO) and characterized by ^{29}Si{^{1}H} CP/MAS NMR spectroscopy, ^{29}Si MAS NMR spectroscopy and XRD analysis (refer Supplementary Information, S6.3.2). All these three techniques could identify the characteristic features of the conventional M-S-H phase. This strongly supports the claim that a conventional M-S-H phase is not present in AAMs, and that these three techniques as applied here are reliable to the extent that they could have identified the conventional M-S-H phase had it been formed in the AAMs in question.

3.5. SEM analysis of samples

The results of the SEM-EDX analysis of sample A4_1Y are shown in Fig. 9. Some regions of interest are marked with labels. Regions g1 and g2 represent the unreacted glasses. The rims (r_{g1} and r_{g2}) around the unreacted glasses are richer in Si, Mg, and O, thereby indicating formation of some form of magnesium silicate phase in apparent alteration layers on the glass particle surfaces. Previous analysis by XRD (Fig. 3) and ^{29}Si MAS NMR analysis (Section 3.4) ruled out the existence of M-S-H or crystalline magnesium silicate phases. This strongly suggests that the region constituted by r_{g1} and r_{g2} represent an amorphous magnesium silicate (AMS) phase. Regions p1, p2 and p3 are richer in Al and Na, and contains Si and O. These regions represent the zeolite phases identified by XRD (Fig. 3) analysis and confirmed by ^{29}Si MAS NMR analysis (Section 3.4). The rims (r_{p1} $r_{p2,}$ and r_{p3}) surrounding these zeolite phases are richer in Mg, Si and O. These regions represent the AMS phase.

Analysis of A4_1Y performed with higher magnification is shown in Fig. 10. Here some regions, which are already identified in the lower magnification images, can be observed with better clarity. The AMS phase, beside existing as rims around zeolite and unreacted glass, also exists as individual regions, as represented by x1. Regions such as s1 and s2 are richer in Na, C and O, corresponding to the thermonatrite identified by XRD (Fig. 3). Note that thermonatrite cannot be quantified in this analysis, as it can be easily lost during SEM sample preparation.

The distribution of the network modifying cations (Na and Mg), as seen in SEM-EDX images of A4_1Y (Figs. 9 and 10), can be explained using the cation charge density. The cation charge density is known to play an important role in distribution of network modifying cations in aluminosilicate systems [24]. The cation charge density can be expressed in the form of cation field strength, CFS = Z/r^2, where Z = cation charge, and r = cation radius in Å. The CFS for Mg is 0.46 Å^{-2}, while for Na it is 0.18 Å^{-2} [36]. In an aluminosilicate system, like A4_1Y in this case, network modifying cations need to perform two important functions: charge balancing the negative charge associated with depolymerized silicate species (Q$^{0-3}$(mAl)); and charge balancing the negative charge associated with the tetrahedral alumina. The negative charge associated with depolymerized silicate species arises from non-bridging oxygen (NBO) while the negative charge associated with tetrahedral aluminum is originating from bridging oxygen (BO) [24]. NBO carries

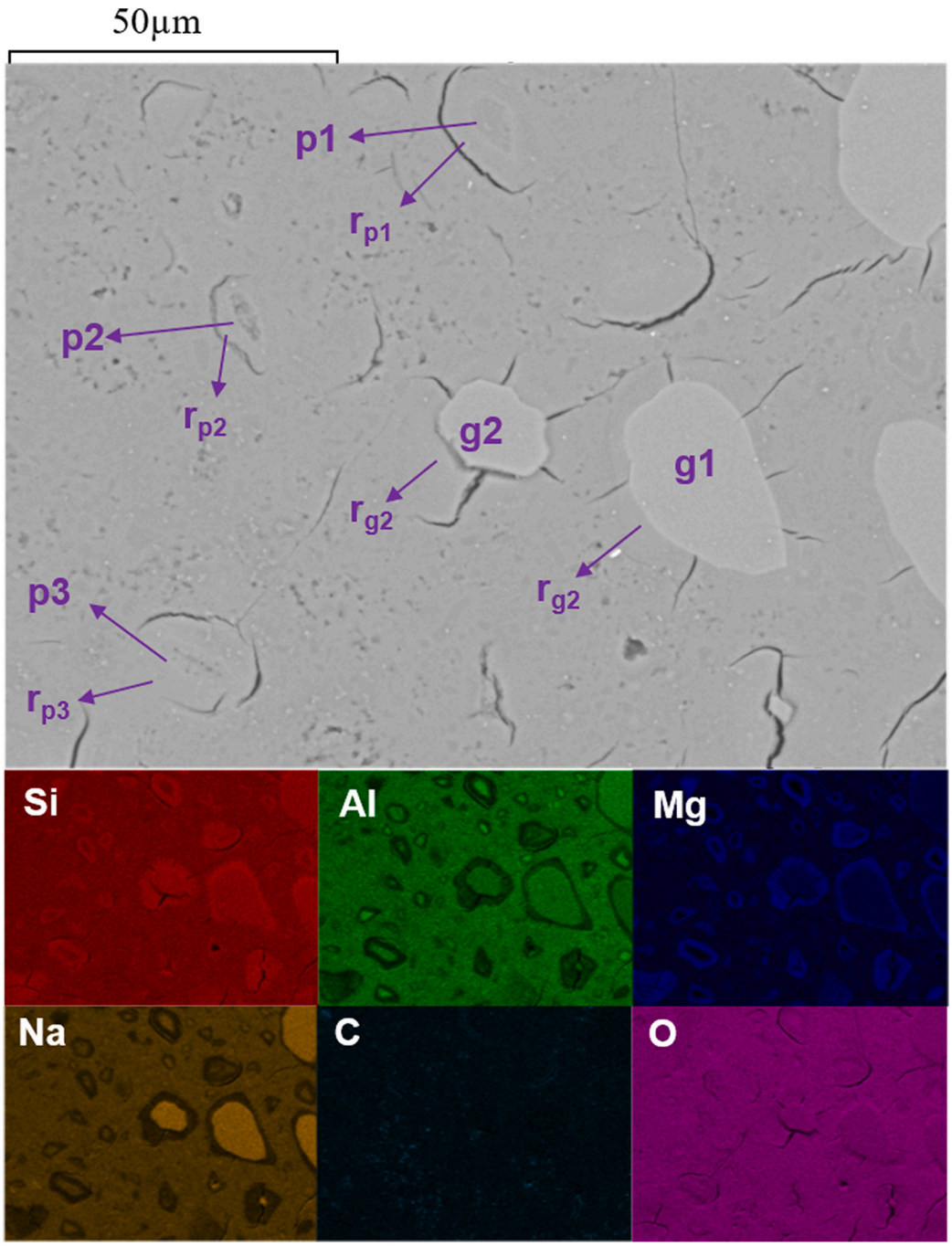

Fig. 9. SEM (low magnification) analysis of A4_1Y.

higher negative charge density than BO [24]. A high charge density negative ion can be better stabilized by a high charge density positive ion. Hence Mg, when compared to Na, can more effectively stabilize the NBO associated with the depolymerized silicate species. Conversely, Na, with low charge density, can effectively stabilize the BO associated with aluminate tetrahedra, particularly those which form part of zeolitic structures. This leads to preferential distribution of Na in zeolitic phases, while the Mg preferentially associates with depolymerized silicate species, leading to the formation of the AMS phase. The Na/Mg mole ratio of A4_1Y is 5.15 including Na contributed by the activating solution. Despite the large excess of Na when compared to Mg, Na does not associate with depolymerized silicate species. Rather, the excess Na appeared as thermonatrite, as indicated by XRD (Fig. 3). This signifies the considerable influence of cation charge density on the distribution of Na and Mg in AAM. In short, it can be concluded that the higher charge density of Mg than Na drives the formation of the AMS phase in AAM.

The possibility of existence in AAMs of an amorphous magnesium silicate phase other than conventional M-S-H was first indicated by the results of Walkley et al. [17]. Those authors studied AAMs within the $CaO\text{-}MgO\text{-}Na_2O\text{-}Al_2O_3\text{-}SiO_2$ regime, and identified hydrotalcite as the key Mg-containing phase formed in AAMs. However, while plotting the Mg:Al molar ratios based on ESEM-EDX spot analysis, those authors observed that this ratio in some AAMs was significantly higher than could be accommodated by a hydrotalcite phase. This led those authors to suggest the possibility that Mg was present in an amorphous magnesium silicate phase, in addition to the Mg-containing hydrotalcite, as they could not find evidence for the presence of M-S-H, brucite, or Mg-carbonate phases in the AAMs.

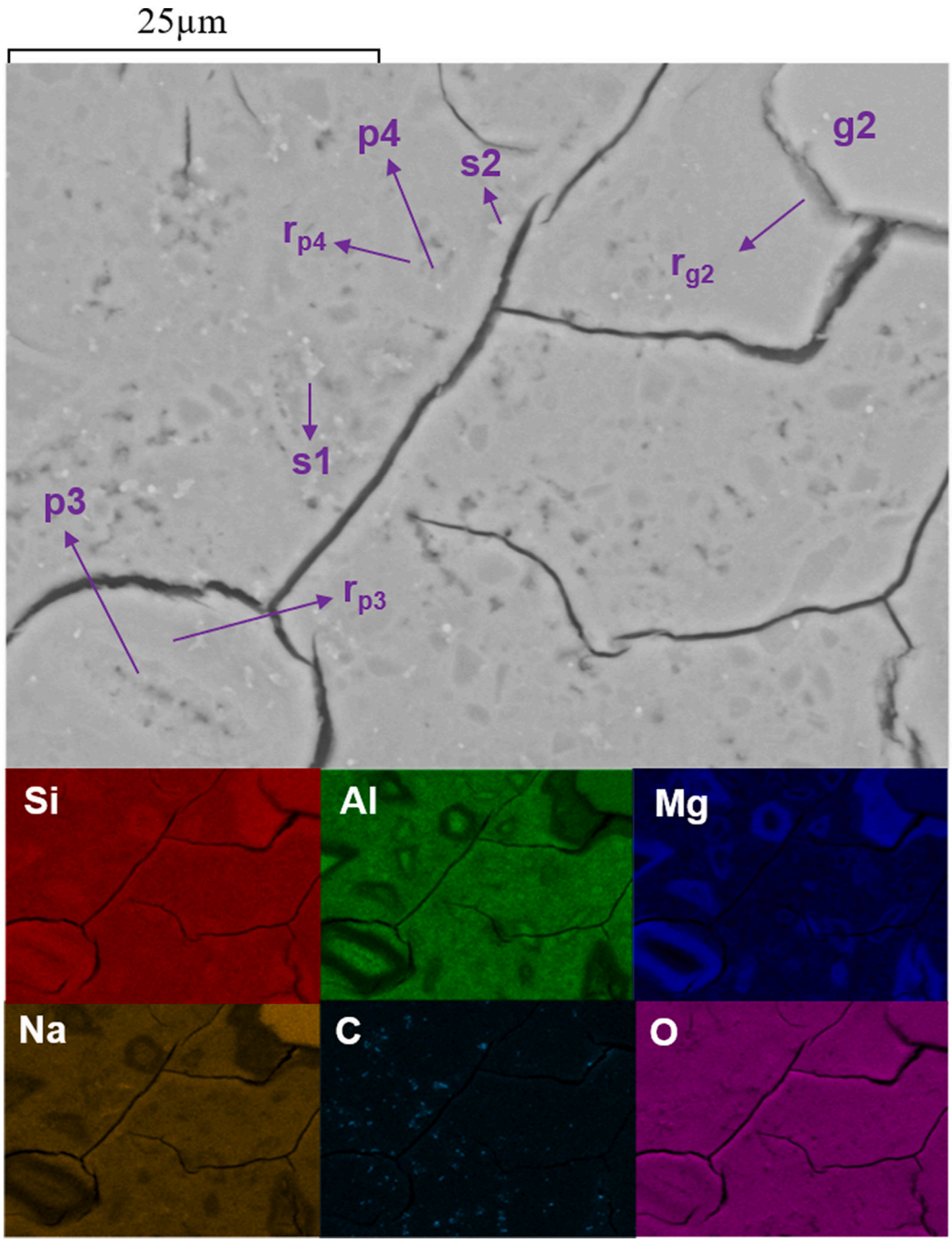

Fig. 10. SEM (high magnification) analysis of A4_1Y.

The results of the SEM-EDX analysis of sample A5_1Y are shown in Supplementary Information, Fig. SF7.1. The regions representing unreacted glass, AMS phase, and zeolite phase can be identified in the figure. However, this identification is made easier by using a high magnification analysis of the same sample (Fig. 11). The unreacted glasses are represented by g4, g5 and g6. The rims (r_{g4}, r_{g5} and r_{g6}) surrounding unreacted glasses are enriched only in Si, Mg, and O, thereby indicating the presence of an AMS phase. The region p5 represents a zeolitic phase, which is surrounded by a rim r_{p5} (which corresponds to an AMS phase). The regions marked x2 and x3 represent the AMS phase.

The results of the SEM-EDX analysis of sample A6_1Y are shown in Supplementary Information, Fig. SF7.2. The following regions can be identified in this figure: g7 representing unreacted glass; p6 indicating an almost completely reacted glass; a rim (r_{p6}) which represents the AMS phase; and s2 corresponding to thermonatrite. Unlike in case of A4_1Y and A5_1Y, the sample A6_1Y exhibits poor distinction between zeolitic and AMS phases. This could be due to the fact that on moving from A4_1Y to A6_1Y, the proportion of highly depolymerized silicate species (which mostly constitute AMS) drops from 60% to 32% (refer Section 3.4, ^{29}Si MAS NMR data). The AMS and zeolitic phases exist together in this AAM, thereby making their individual identification difficult. The identification between phases is also difficult in the high magnification analysis of the same sample (Fig. 12), which could not specifically show any zeolite-rich region. However, it could show regions x4 and x5, which are identified as AMS, and region s3 which corresponds to thermonatrite.

The results of the SEM-EDX analysis of sample A9_1Y is shown in

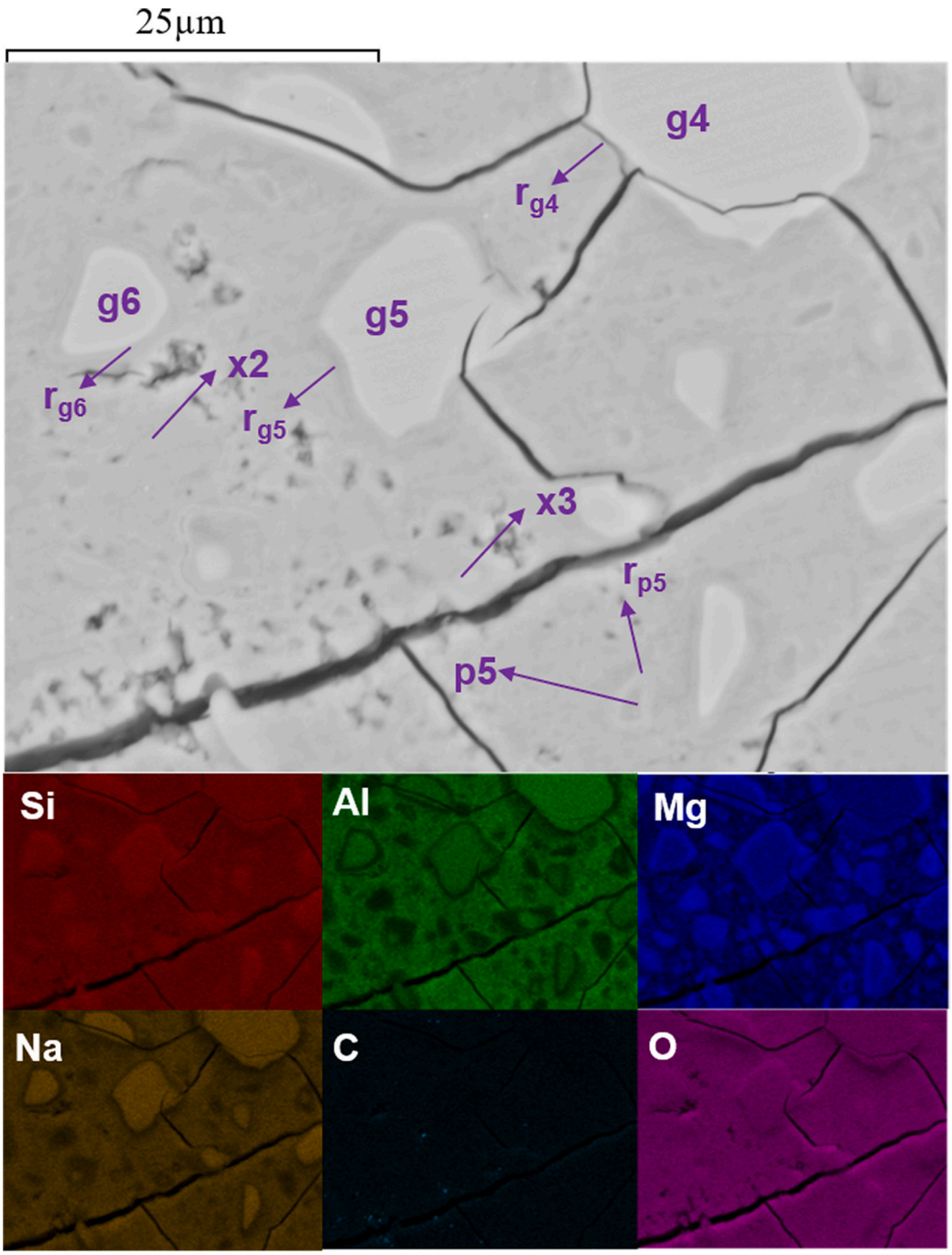

Fig. 11. SEM (high magnification) analysis of A5_1Y.

Fig. 13. Although unreacted glass (g8, g9, and g10) as well as product phases (p7, p8, p9) are clearly seen, there is no visible distinction between zeolitic and AMS phases. The proportion of highly depolymerized silicate species (which mostly constitute AMS) in this sample is around 15% (refer Section 3.4 ^{29}Si MAS NMR). The AMS and zeolitic phases coexist together in this AAM.

None of the AAMs exhibited the following regions: 1) rich in Mg, Al and O only (which would indicate hydrotalcite-group phases); 2) rich in Mg and O only (which would correspond to brucite); 3) rich in Mg, C and O only (which would represent magnesium (hydroxy) carbonates). Rather, the analysis of AAMs indicates regions rich in Si, Mg and O only. This corresponds to an amorphous magnesium silicate (AMS), since the existence of M-S-H or crystalline magnesium silicate phases was ruled out by XRD (Fig. 3) and ^{29}Si MAS NMR analyses (Section 3.4).

3.6. TG-MS analysis of samples

The results of the TG-MS analysis of AAMs are shown in Fig. 14. The sample A4_1Y shows mass loss around 100 °C which corresponds to molecular water associated with products such as zeolites, as well as pore fluid. There is a second mass loss spanning from 500 °C to 600 °C, which corresponds to release of CO_2. This could be due to decomposition of thermonatrite, the only carbonate phase identified by XRD and SEM analysis. Although thermonatrite decomposition usually takes place at 800 °C, the presence of other species in the system can lower the decomposition temperature [37]. The sample A7_1Y shows a mass loss around 100 °C, which is lower when compared to the corresponding feature observed for A4_1Y. This is due to the lower reactivity of glass G7, which leads to less products and hence, less molecular water. In

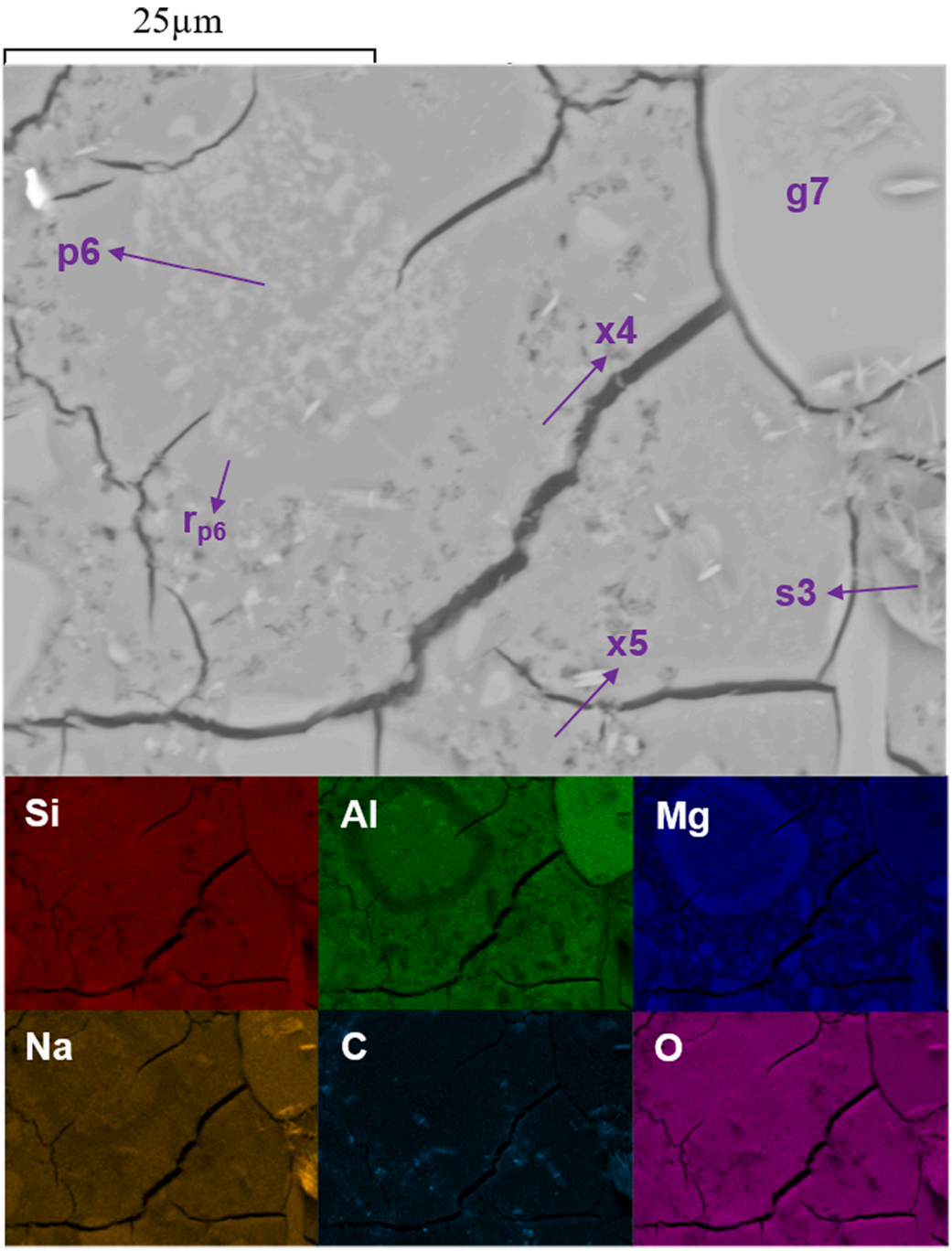

Fig. 12. SEM (high magnification) analysis of A6_1Y.

sample A10_1Y, the mass loss around 100 °C is the lowest among all AAMs.

The TG-MS analysis of the AAMs can be used to rule out the existence of the following Mg-containing phases: hydrotalcite, brucite, and the conventional M-S-H phase. If hydrotalcite is formed, it will exhibit a first decomposition peak close to 180 °C, and a second decomposition spanning from 270 °C to 390 °C [38]. Brucite, if present, will give a decomposition peak around 400 °C [39]. The M-S-H phase would decompose at around 550 °C [40] and contribute to the water signal. The absence of hydrotalcite, brucite, and the M-S-H phase, as concluded from TG-MS analysis, also agrees with XRD, ^{27}Al NMR, ^{29}Si NMR, and the SEM analysis of AAMs.

Conversely, Fig. 15 shows the TG-MS analysis of the solid residue (R10_1D) from the alkaline dissolution of glass G10. It shows a mass loss around 100 °C, which corresponds to molecular water associated with hydrotalcite. The mass losses at 190 °C, 300 °C, and 375 °C correspond to decomposition of hydrotalcite. These observations agree with XRD and ^{27}Al NMR analysis (Figs. 4 and 6), which clearly indicated the presence of hydrotalcite-group phases.

4. Conclusions

The main product formed during the alkali activation of Na—Mg aluminosilicate glasses after extended curing is zeolitic in nature. No hydrotalcite phase is formed, as Al is preferentially incorporated into zeolites. The dominant zeolite phases (LSX and garronite) formed in AAMs have a Si:Al ratio of 1, while all the glass precursors have similar Si:Al ratio of 2.5. This means that during the formation of zeolite from

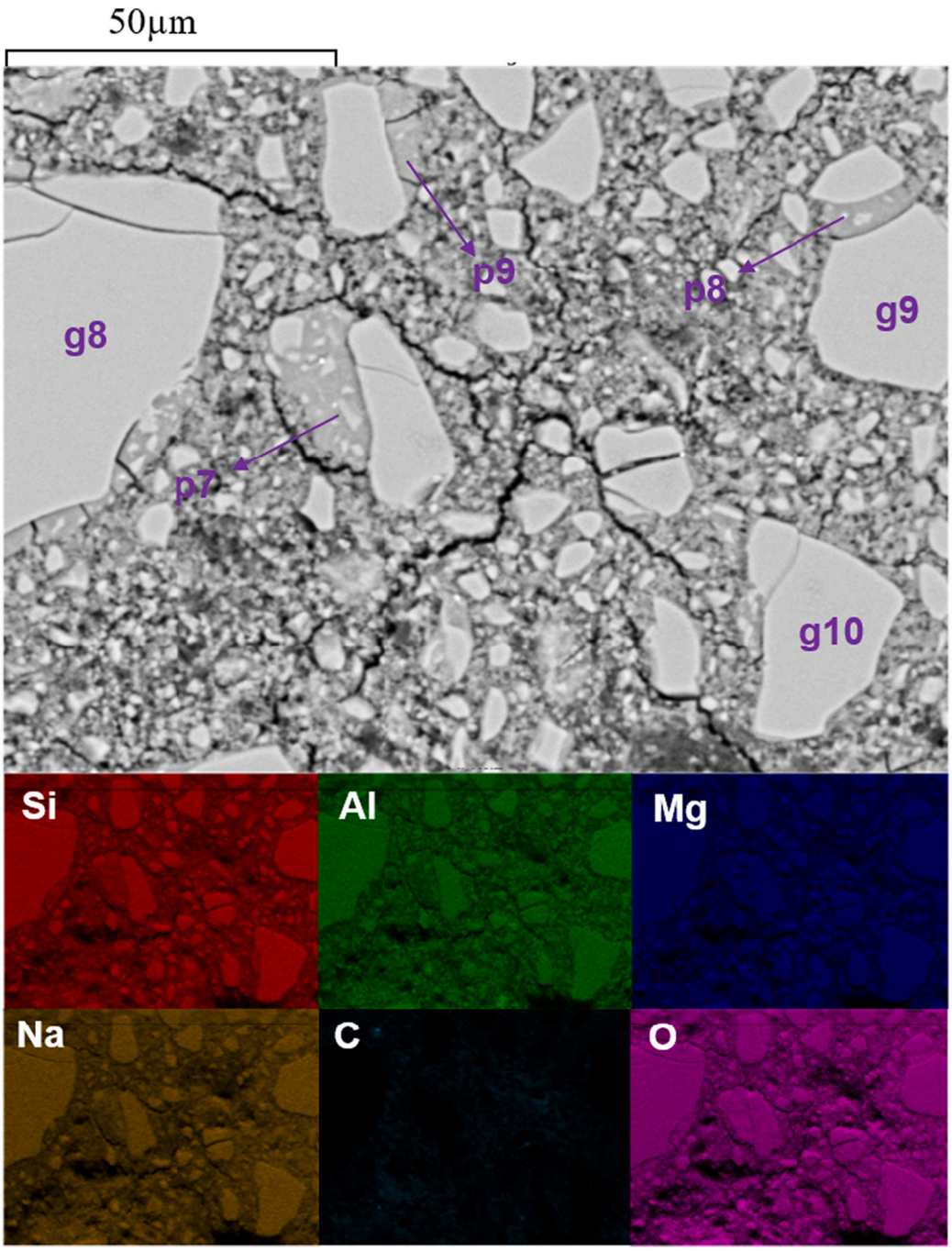

Fig. 13. SEM (low magnification) analysis of A9_1Y.

glass precursors, Al is the limiting reactant, thereby leaving no Al available for hydrotalcite formation. Detailed characterization by various techniques produced no evidence for formation of brucite, magnesium (hydroxy-)carbonates, or conventional magnesium silicate hydrate (M-S-H) phases in the AAMs. The Mg in AAMs is instead observed to form an amorphous magnesium silicate (AMS) phase, a fate of Mg which is not well reported in the literature studies focusing on Mg-rich AAMs. The formation of AMS may be driven by the fact that the high positive charge density of Mg (compared to Na) can effectively stabilize the high negative charge density of the non-bridging oxygen (NBO) associated with the depolymerized silicate species (Q^{0-3}(*m*Al)). The existence of AMS should be considered as a possible fate for Mg in Mg-containing AAMs, especially in complex systems, where its identification may be difficult.

CRediT authorship contribution statement

Harisankar Sreenivasan: Formal analysis, Investigation, Methodology, Conceptualization Visualization, Writing - original draft, Writing - review & editing. *Elijah Adesanya*: Investigation, Methodology, Writing - review & editing. *He Niu*: Investigation, Methodology, Writing - review & editing. *Priyadharshini Perumal*: Methodology, Writing - review & editing. *Anu M. Kantola*: Investigation, Methodology, Writing - review & editing. *Ville-Veikko Telkki*: Investigation, Methodology, Writing - review & editing. *Marko Huttula*: Funding acquisition, Writing - review & editing. *Wei Cao*: Supervision, Funding acquisition, Writing - review & editing *Mirja Illikainen*: Supervision, Funding acquisition, Writing - review & editing. *John* L. *Provis*: Conceptualization, Validation, Methodology, Supervision, Writing - review & editing. *Paivo Kinnunen*:

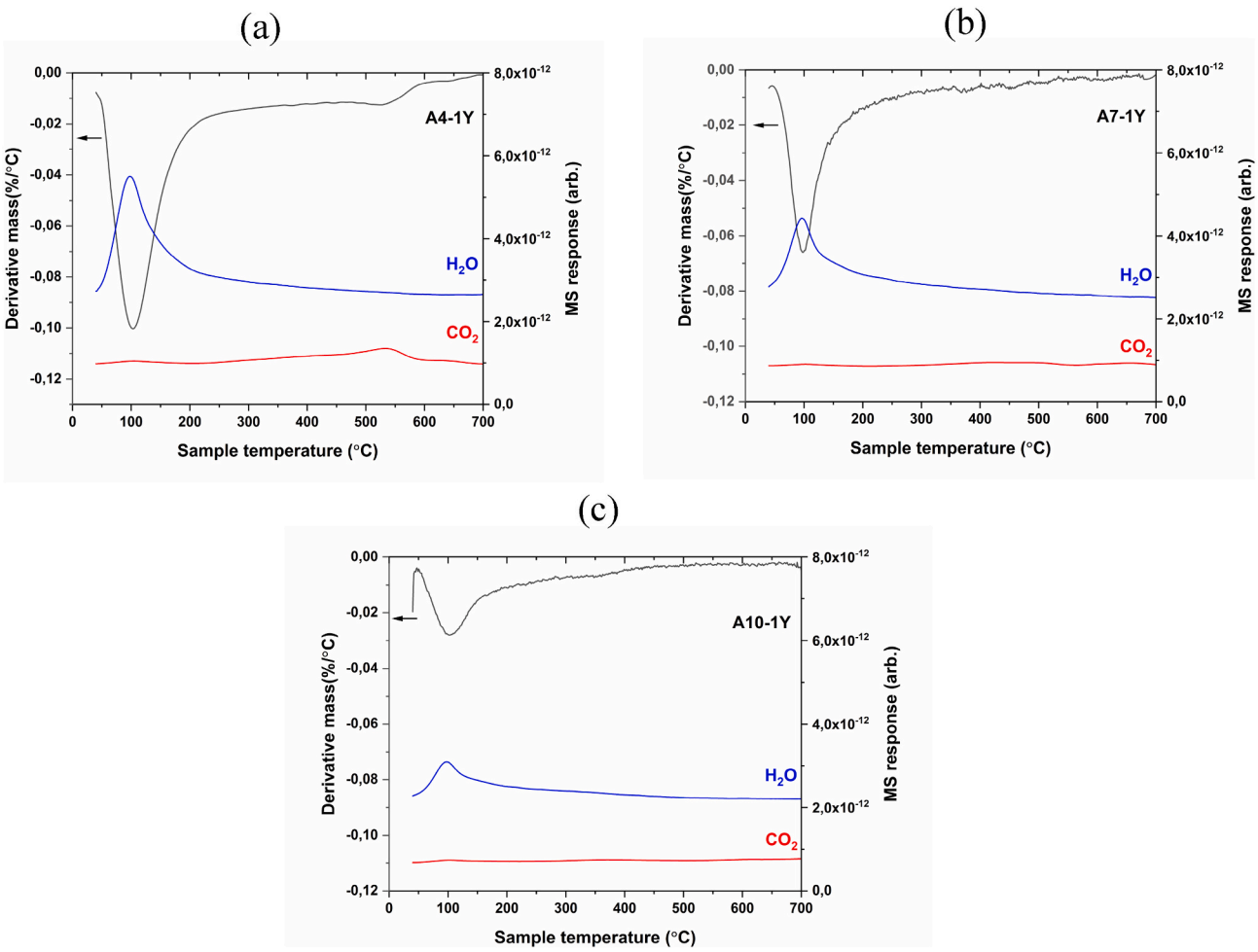

Fig. 14. TG-MS analysis of AAMs: (a) A4_1Y, (b) A7_1Y, and (c) A10_1Y.

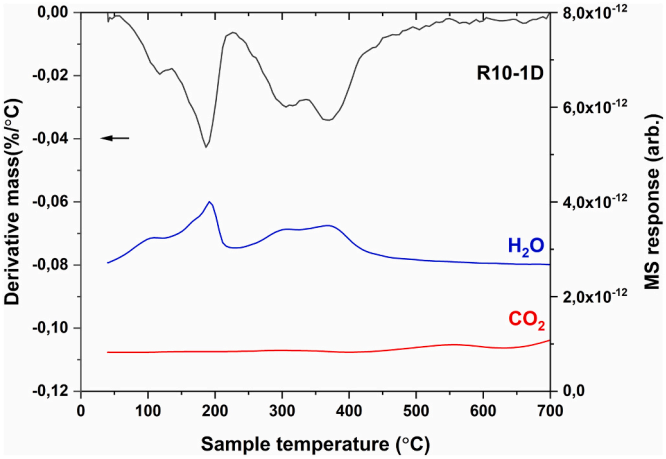

Fig. 15. TG-MS analysis of solid residue (R10_1D) from alkaline dissolution of glasses.

Conceptualization, Validation, Methodology, Funding acquisition, Supervision, Writing - review & editing.

Declaration of competing interest

The authors declare that they have no known competing financial interests or personal relationships that could have appeared to influence the work reported in this paper.

Acknowledgements

The authors gratefully acknowledge the financial support received from the European Union's Horizon 2020 research and innovation programme under the Marie Skłodowska-Curie COFUND Grant Agreement no. 713606 (I4FUTURE). P.K. acknowledges financial support from Kvantum institute (University of Oulu) and Academy of Finland (grants 322085, 329477 and 326291). A.M.K and V.-V.T. acknowledge the financial support from Kvantum institute (University of Oulu) and Academy of Finland (grants #289649 and 319216). The authors would also like to thank Marcin Selent for his help with XRD measurement, Pasi Juntunen with SEM measurement and Tommi Kokkonen with glass synthesis and TG-MS measurements. This work/part of the work was carried out with the support of the Centre for Material Analysis, University of Oulu, Finland.

Appendix A. Supplementary data

Alkaline reactivity of (Na-Mg) aluminosilicate glasses; Appearance of AAMs after milling; XRD analysis of the solid residues obtained during alkaline dissolution experiments; TEM analysis of the solid residues obtained during alkaline dissolution experiments; The chemical shifts and FWHM assignments used in the decomposition of the ^{29}Si MAS NMR spectra of AAMs; Additional experiments to explore the possible presence of conventional M-S-H phase in AAMs; SEM images of AAMs. Supplementary data to this article can be found online at https://doi.

org/10.1016/j.cemconres.2021.106464.

References

[1] J.L. Provis, J.S.J. van Deventer, Alkali Activated Materials: State-of-the-Art Report, RILEM TC 224-AAM, Springer/RILEM, Dordrecht, 2014, https://doi.org/10.1007/978-94-007-7672-2.

[2] J.L. Provis, Alkali-activated materials, Cem. Concr. Res. 114 (2018) 40–48, https://doi.org/10.1016/j.cemconres.2017.02.009.

[3] M. Ben Haha, B. Lothenbach, G. Le Saout, F. Winnefeld, Influence of slag chemistry on the hydration of alkali-activated blast-furnace slag — part I: effect of MgO, Cem. Concr. Res. 41 (2011) 955–963, https://doi.org/10.1016/j.cemconres.2011.05.002.

[4] S.A. Bernal, R. San Nicolas, R.J. Myers, R. Mejía de Gutiérrez, F. Puertas, J.S.J. van Deventer, J.L. Provis, MgO content of slag controls phase evolution and structural changes induced by accelerated carbonation in alkali-activated binders, Cem. Concr. Res. 57 (2014) 33–43, https://doi.org/10.1016/j.cemconres.2013.12.003.

[5] X. Ke, S.A. Bernal, J.L. Provis, Uptake of chloride and carbonate by Mg-Al and Ca-Al layered double hydroxides in simulated pore solutions of alkali-activated slag cement, Cem. Concr. Res. 100 (2017) 1–13, https://doi.org/10.1016/j.cemconres.2017.05.015.

[6] F. Jin, K. Gu, A. Al-Tabbaa, Strength and drying shrinkage of reactive MgO modified alkali-activated slag paste, Constr. Build. Mater. 51 (2014) 395–404, https://doi.org/10.1016/j.conbuildmat.2013.10.081.

[7] S.A. Walling, J.L. Provis, Magnesia-based cements: a journey of 150 years, and cements for the future? Chem. Rev. 116 (2016) 4170–4204, https://doi.org/10.1021/acs.chemrev.5b00463.

[8] Y. Chen, J. Wei, Hydrated magnesium silicate system gelling material coagulating and hardening at normal temperature and its preparation method, Chinese Patent CN1267374 C, 2006. https://patents.google.com/patent/CN1594195A/en (accessed August 15, 2020).

[9] S.A. Walling, H. Kinoshita, S.A. Bernal, N.C. Collier, J.L. Provis, Structure and properties of binder gels formed in the system $Mg(OH)_2$–SiO_2–H_2O for immobilisation of Magnox sludge, Dalton Trans. 44 (2015) 8126–8137, https://doi.org/10.1039/C5DT00877H.

[10] T. Zhang, C.R. Cheeseman, L.J. Vandeperre, Development of low pH cement systems forming magnesium silicate hydrate (M-S-H), Cem. Concr. Res. 41 (2011) 439–442, https://doi.org/10.1016/j.cemconres.2011.01.016.

[11] N. Mobasher, S.A. Bernal, J.L. Provis, Structural evolution of an alkali sulfate activated slag cement, J. Nucl. Mater. 468 (2016) 97–104, https://doi.org/10.1016/j.jnucmat.2015.11.016.

[12] A. Buchwald, H. Hilbig, Ch. Kaps, Alkali-activated metakaolin-slag blends—performance and structure in dependence of their composition, J. Mater. Sci. 42 (2007) 3024–3032, https://doi.org/10.1007/s10853-006-0525-6.

[13] A.F. Abdalqader, F. Jin, A. Al-Tabbaa, Characterisation of reactive magnesia and sodium carbonate-activated fly ash/slag paste blends, Constr. Build. Mater. 93 (2015) 506–513, https://doi.org/10.1016/j.conbuildmat.2015.06.015.

[14] S.A. Walling, S.A. Bernal, L.J. Gardner, H. Kinoshita, J.L. Provis, Blast furnace slag-$Mg(OH)_2$ cements activated by sodium carbonate, RSC Adv. 8 (2018) 23101–23118, https://doi.org/10.1039/C8RA03717E.

[15] O. Burciaga-Díaz, I. Betancourt-Castillo, Characterization of novel blast-furnace slag cement pastes and mortars activated with a reactive mixture of MgO-NaOH, Cem. Concr. Res. 105 (2018) 54–63, https://doi.org/10.1016/j.cemconres.2018.01.002.

[16] J. Yliniemi, B. Walkley, J.L. Provis, P. Kinnunen, M. Illikainen, Nanostructural evolution of alkali-activated mineral wools, Cem. Concr. Compos. 106 (2020) 103472, https://doi.org/10.1016/j.cemconcomp.2019.103472.

[17] B. Walkley, R. San Nicolas, M.-A. Sani, S.A. Bernal, J.S.J. van Deventer, J.L. Provis, Structural evolution of synthetic alkali-activated CaO-MgO-Na_2O-Al_2O_3-SiO_2 materials is influenced by Mg content, Cem. Concr. Res. 99 (2017) 155–171, https://doi.org/10.1016/j.cemconres.2017.05.006.

[18] Y. Chen, Z. Shui, W. Chen, Q. Li, G. Chen, Effect of MgO content of synthetic slag on the formation of Mg-Al LDHs and sulfate resistance of slag-fly ash-clinker binder, Constr. Build. Mater. 125 (2016) 766–774, https://doi.org/10.1016/j.conbuildmat.2016.08.086.

[19] T. Yang, Z. Zhang, H. Zhu, X. Gao, C. Dai, Q. Wu, Re-examining the suitability of high magnesium nickel slag as precursors for alkali-activated materials, Constr. Build. Mater. 213 (2019) 109–120, https://doi.org/10.1016/j.conbuildmat.2019.04.063.

[20] S.A. Walling, S.A. Bernal, L.J. Gardner, H. Kinoshita, J.L. Provis, Phase formation and evolution in $Mg(OH)_2$–zeolite cements, Ind. Eng. Chem. Res. 57 (2018) 2105–2113, https://doi.org/10.1021/acs.iecr.7b04201.

[21] T. Yang, X. Yao, Z. Zhang, Geopolymer prepared with high-magnesium nickel slag: characterization of properties and microstructure, Constr. Build. Mater. 59 (2014) 188–194, https://doi.org/10.1016/j.conbuildmat.2014.01.038.

[22] P. Kinnunen, J. Yliniemi, B. Talling, M. Illikainen, Rockwool waste in fly ash geopolymer composites, J. Mater. Cycles Waste Manag. 19 (2017) 1220–1227, https://doi.org/10.1007/s10163-016-0514-z.

[23] Y.J. Zhang, Y.L. Zhao, H.H. Li, D.L. Xu, Structure characterization of hydration products generated by alkaline activation of granulated blast furnace slag, J. Mater. Sci. 43 (2008) 7141–7147, https://doi.org/10.1007/s10853-008-3028-9.

[24] H. Sreenivasan, P. Kinnunen, E. Adesanya, M. Patanen, A.M. Kantola, V.-V. Telkki, M. Huttula, W. Cao, J.L. Provis, M. Illikainen, Field strength of network modifying cation dictates the structure of (Na-Mg) aluminosilicate glasses, Front. Mater. 7 (2020) 267, https://doi.org/10.3389/fmats.2020.00267.

[25] H. Sreenivasan, W. Cao, Y. Hu, Q. Xiao, M. Shakouri, M. Huttula, J.L. Provis, M. Illikainen, P. Kinnunen, Towards designing reactive glasses for alkali activation: understanding the origins of alkaline reactivity of Na-Mg aluminosilicate glasses, PLoS One 15 (2020), e0244621, https://doi.org/10.1371/journal.pone.0244621.

[26] N.K. Nasikas, A. Chrissanthopoulos, N. Bouropoulos, S. Sen, G.N. Papatheodorou, Silicate glasses at the ionic limit: alkaline-earth sub-orthosilicates, Chem. Mater. 23 (2011) 3692–3697, https://doi.org/10.1021/cm2012582.

[27] B. Lothenbach, D. Nied, E. L'Hôpital, G. Achiedo, A. Dauzères, Magnesium and calcium silicate hydrates, Cem. Concr. Res. 77 (2015) 60–68, https://doi.org/10.1016/j.cemconres.2015.06.007.

[28] S.K. Lee, J.F. Stebbins, The structure of aluminosilicate glasses: high-resolution ^{17}O and ^{27}Al MAS and 3QMAS NMR study, J. Phys. Chem. B 104 (2000) 4091–4100, https://doi.org/10.1021/jp994273w.

[29] S.K. Lee, H.-I. Kim, E.J. Kim, K.Y. Mun, S. Ryu, Extent of disorder in magnesium aluminosilicate glasses: insights from ^{27}Al and ^{17}O NMR, J. Phys. Chem. C 120 (2016) 737–749, https://doi.org/10.1021/acs.jpcc.5b10799.

[30] G. Engelhardt, Chapter 9, solid state NMR spectroscopy applied to zeolites, in: H. van Bekkum, E.M. Flanigen, P.A. Jacobs, J.C. Jansen (Eds.), Studies in Surface Science and Catalysis, Elsevier, 2001, pp. 387–418, https://doi.org/10.1016/S0167-2991(01)80251-2.

[31] B. Walkley, J.L. Provis, Solid-state nuclear magnetic resonance spectroscopy of cements, Mater. Today Adv. 1 (2019) 100007, https://doi.org/10.1016/j.mtadv.2019.100007.

[32] P. Faucon, T. Charpentier, D. Bertrandie, A. Nonat, J. Virlet, J.C. Petit, Characterization of calcium aluminate hydrates and related hydrates of cement pastes by ^{27}Al MQ-MAS NMR, Inorg. Chem. 37 (1998) 3726–3733, https://doi.org/10.1021/ic9800076.

[33] S.A. Bernal, J.L. Provis, B. Walkley, R. San Nicolas, J.D. Gehman, D.G. Brice, A. R. Kilcullen, P. Duxson, J.S.J. van Deventer, Gel nanostructure in alkali-activated binders based on slag and fly ash, and effects of accelerated carbonation, Cem. Concr. Res. 53 (2013) 127–144, https://doi.org/10.1016/j.cemconres.2013.06.007.

[34] J. Mahler, A. Sebald, Deconvolution of ^{29}Si magic-angle spinning nuclear magnetic resonance spectra of silicate glasses revisited — some critical comments, Solid State Nucl. Magn. Reson. 5 (1995) 63–78, https://doi.org/10.1016/0926-2040(95)00027-N.

[35] D. Nied, K. Enemark-Rasmussen, E. L'Hopital, J. Skibsted, B. Lothenbach, Properties of magnesium silicate hydrates (M-S-H), Cem. Concr. Res. 79 (2016) 323–332, https://doi.org/10.1016/j.cemconres.2015.10.003.

[36] A. Quintas, D. Caurant, O. Majérus, T. Charpentier, J.-L. Dussossoy, Effect of the nature of alkali and alkaline-earth oxides on the structure and crystallization of an aluminoborosilicate glass developed to immobilize highly concentrated nuclear waste solutions, in: International Conference Atalante 2008. Nuclear Fuel Cycles for a Sustainable Future, Montpellier: France, 2008. http://arxiv.org/abs/0912.1576.

[37] R.V. Siriwardane, J.A. Poston, C. Robinson, T. Simonyi, Effect of additives on decomposition of sodium carbonate: precombustion CO_2 capture sorbent regeneration, Energy Fuel 25 (2011) 1284–1293, https://doi.org/10.1021/ef101486m.

[38] F. Rey, V. Fornés, J.M. Rojo, Thermal decomposition of hydrotalcites. An infrared and nuclear magnetic resonance spectroscopic study, J. Chem. Soc. Faraday Trans. 88 (1992) 2233–2238, https://doi.org/10.1039/FT9928802233.

[39] K.J.D. MacKenzie, R.H. Meinhold, Thermal decomposition of brucite, $Mg(OH)_2$: a ^{25}Mg MAS NMR study, Thermochim. Acta 230 (1993) 339–343, https://doi.org/10.1016/0040-6031(93)80371-G.

[40] S.A. Walling, H. Kinoshita, S.A. Bernal, N.C. Collier, J.L. Provis, Structure and properties of binder gels formed in the system $Mg(OH)_2$–SiO_2–H_2O for immobilisation of Magnox sludge, Dalton Trans. 44 (2015) 8126–8137, https://doi.org/10.1039/C5DT00877H.